

Supporting Information

NH₃ and HNO_x Formation and Loss in Nitrogen Fixation from Air with Water Vapor by Nonequilibrium Plasma

Elise Vervloessem^{†,‡,}, Mikhail Gromov^{‡,†}, Nathalie De Geyter[‡], Annemie Bogaerts[†], Yury*

Gorbanev^{†,x}, Anton Nikiforov^{‡,x}

[†]Research group PLASMANT, Department of Chemistry, University of Antwerp,

Universiteitsplein 1, 2610 Wilrijk, Belgium

[‡]Research Unit Plasma Technology (RUPT), Department of Applied Physics, Ghent

University, Sint-Pietersnieuwstraat 41, 9000 Ghent, Belgium

[†]Chimie des Interactions Plasma Surface (ChiPS), CIRMAP, Mons University, 20 Place du

Parc, 7000 Mons, Belgium

*elise.vervloessem@uantwerpen.be

Pages: 24

Figures: 5

Tables: 6

Contents

<i>S1. Schematic of the plasma device</i>	s3
Figure S1. Various pathways for plasma-based nitrogen fixation with a focus on the different possible hydrogen sources. The current industrial process is shown as a reference in blue. Each full line represents a possible pathway towards basic fertilizer chemicals.....	s3
<i>S2. Schematic of the plasma device</i>	s3
Figure S2. Schematic of the plasma device. HV stands for high voltage electrode.	s3
<i>S3. FTIR analysis</i>	s4
Figure S3. (a) Overview of absorption bands from NO, NO ₂ , N ₂ O, HNO ₃ , HNO ₂ , NH ₃ and O ₃ . (b) HNO ₂ and HNO ₃ bands in the 3400 – 3800 cm ⁻¹ region. (c) HNO ₂ , HNO ₃ , NO and NO ₂ bands in the 1550 – 1850 cm ⁻¹ region. (d) HNO ₂ and HNO ₃ bands in the 1100 - 1500 cm ⁻¹ region. (e) HNO ₂ and HNO ₃ bands in the 700 - 1100 cm ⁻¹ region. All simulated spectra have been taken from the HITRAN database ¹ , except for HNO ₂ and the HNO ₃ region 3700 – 3800 cm ⁻¹ annotated with dashed lines, which were digitized from Pipa et al. ⁶ based on literature values. ^{7,8}	s5
<i>S4. Experimental setups of OES</i>	s5
Figure S4. Basic gas analysis experimental setup as explained in the main text. (a) OES setup axial to the jet. (b) OES setup perpendicular to the afterglow using 10 fibers for spatially resolved measurements (1-10 mm from the nozzle).	s5
<i>S5. Optical emission spectroscopy</i>	s5
S5.1. Correction for quenching by H ₂ O, O ₂ and N ₂	s6
Table S1. Einstein transitions coefficients of NH(A ³ Π-X ³ Σ) and NO(A ² Σ ⁺).....	s7
Table S2. The cross sections and rate coefficients for NH(A ³ Π) and NO(A ² Σ ⁺) quenching by N ₂ , O ₂ and H ₂ O as collisional quenchers.....	s7
S5.2 Correction for sensitivity	s7
S5.3 Correction for excitation probability.....	s7
<i>S6. NO_x formation in (humid) N₂ and air</i>	s8
Table S3. (Extended) Zeldovich reactions, their corresponding reaction rate coefficients and relevant temperature ranges.	s9
<i>S7. OES spectra recorded perpendicular to the plasma effluent</i>	s9
Table S4. Overview of the waterfall plot conditions and their respective Figure numbers.	s9
Figure S5. Emission spectra (334–340 nm) as a function of the distance from the jet nozzle (1–10 mm). The full list of the experimental conditions (Figures S5a – S5t) is shown in Table S3 above.....	s10
<i>S8. Energy consumption and production rate</i>	s20

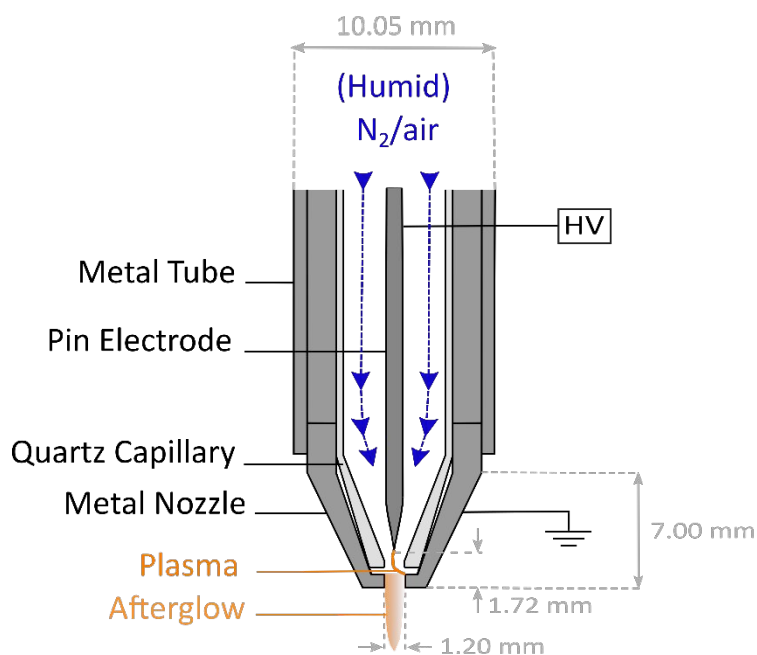


Figure S2. Schematic of the plasma device. HV stands for high voltage electrode.

S3. FTIR analysis

Absorbance spectra measured by Fourier transform infrared spectroscopy revealed the presence of several vibrational transitions which correspond to NO, NO₂, N₂O, NH₃, and HNO₂ species. The Bruker system (with the OPUS gas analysis software) was factory-calibrated for NO, NO₂, N₂O, O₃ and N₂O₅. The remaining peaks were identified using the HITRAN database.¹ Their concentrations were determined by measuring a reference signal from the gas mixture with a known concentration of the species of interest and *via* Beer's law as follows²:

$$n_j = \frac{\ln(I^{(v)}/I_0^{(v)})}{\sigma_j(v) \cdot L} \times \left(\frac{10^{12}}{n}\right) \quad (\text{S1})$$

where $\ln(I^{(v)}/I_0^{(v)})$ is the measured absorbance ($A(v)$) as a function of wavenumber (v), $\sigma_j(v)$ is the absorption cross-section of species j as a function of v [in cm² molecule⁻¹], and L is the length of the absorbance pathway [in cm]. The last term in the brackets performs the unit conversion from (cm⁻³) to (ppm), where n is the gas density at 323 Kelvin (the temperature in the gas cell). This method is commonly used in gas analysis using FTIR.³⁻⁵ Though for NO, NO, NO₂ and N₂O the concentration was determined through both Beer's law and the Bruker system, all concentrations reported are determined using Beer's law, for consistency.

Figure S1 shows the theoretical absorbance peaks for NO, NO₂, N₂O, NH₃, HNO₃, HNO₂ and O₃. Species present in detectable quantities were NO, NO₂, NH₃ and HNO₂, though not at all conditions. The concentration of N₂O was <2 ppm for all conditions measured. HNO₃ was not detected at any of the examined conditions, as well as O₃ due to the relatively high gas temperature of the afterglow.

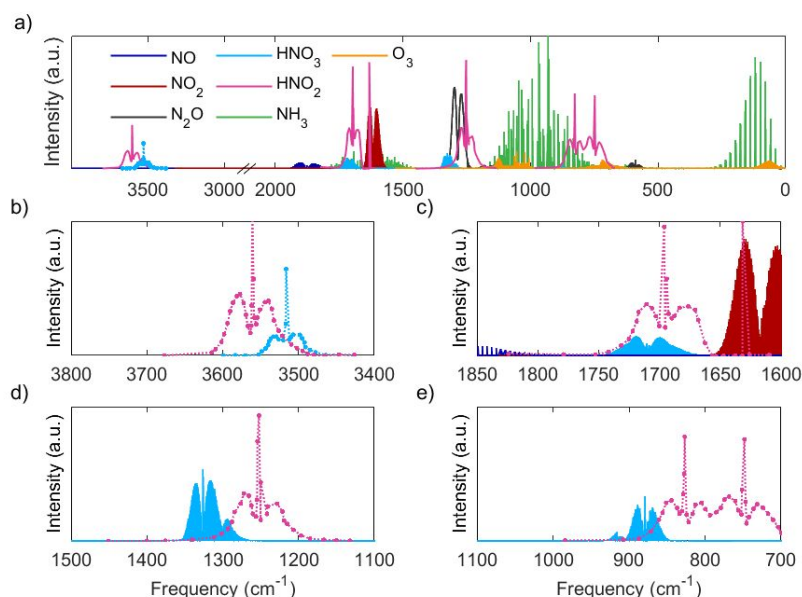


Figure S3. (a) Overview of absorption bands from NO, NO₂, N₂O, HNO₃, HNO₂, NH₃ and O₃. (b) HNO₂ and HNO₃ bands in the 3400 – 3800 cm⁻¹ region. (c) HNO₂, HNO₃, NO and NO₂ bands in the 1550 – 1850 cm⁻¹ region. (d) HNO₂ and HNO₃ bands in the 1100 - 1500 cm⁻¹ region. (e) HNO₂ and HNO₃ bands in the 700 - 1100 cm⁻¹ region. All simulated spectra have been taken from the HITRAN database¹, except for HNO₂ and the HNO₃ region 3700 – 3800 cm⁻¹ annotated with dashed lines, which were digitized from Pipa et al.⁶ based on literature values.^{7,8}

S4. Experimental setups of OES

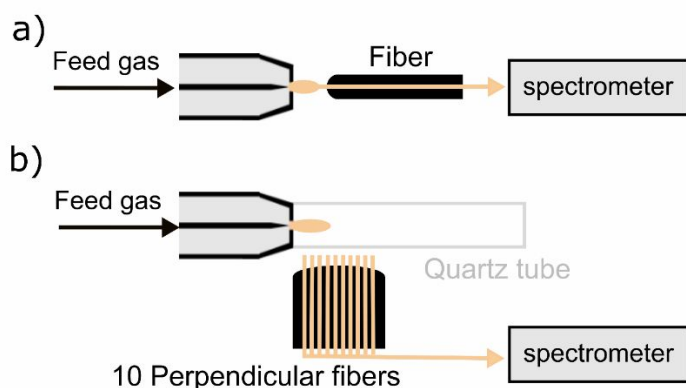


Figure S4. Basic gas analysis experimental setup as explained in the main text. (a) OES setup axial to the jet. (b) OES setup perpendicular to the afterglow using 10 fibers for spatially resolved measurements (1-10 mm from the nozzle).

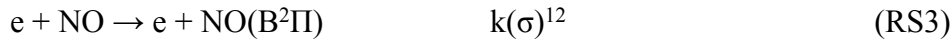
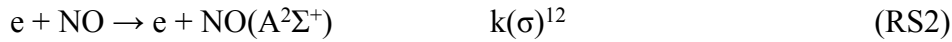
S5. Optical emission spectroscopy

NH(A³Π–X³Σ) can be detected at 336.00 nm; there are no major interferences in this region.

The main pathway for production of $\text{NH}(\text{A}^3\Pi\text{-X}^3\Sigma)$ is through NH_3 . It is commonly accepted that $\text{NH}(\text{A}^3\Pi\text{-X}^3\Sigma)$ is a good indication of the NH_3 density.⁹



The $\text{NO}(\text{A}^2\Sigma^+\text{-B}^2\Pi)$ transition was detected at 226.94 nm. The $\text{NO}(\text{B}^2\Pi\text{-X}^2\Pi)$ transition (around 340 nm¹¹) was only observed in the afterglow. Both $\text{NO}(\text{A}^2\Sigma^+)$ and $\text{NO}(\text{B}^2\Pi)$ states are formed mainly through:



In order to correlate intensities of excited species measured in OES to ground state densities and to compare different bands with each other, a number of corrections and approximations have to be considered as follows:

- (1) Quenching of excited states is taken into account.
- (2) The measured intensities are corrected for the spectrometer sensitivity and fibre optics transparency.
- (3) The signals are corrected to take into account the difference in excitation probabilities associated with the different transitions used. This means the emission of the excited states can be linked to the emission of the ground state.

These corrections have been made under the assumptions of the corona model approximation (explained in sections S5.1-S5.3 below).

S5.1. Correction for quenching by H_2O , O_2 and N_2

Quenching reduces the fraction of the state that can be observed through photon emission¹³ and collisional quenching reduces the effective branching ratio of a spontaneous transition $i \rightarrow k$. Following Hartinger et al.¹⁴, the quenching of the excited species can be expressed as shown in eq. S1. Here q represents the fraction of the excited species that is present after quenching.

$$q = \frac{A}{A+Q}, \text{ where } Q = \sum n_i v_{ri} \sigma_I \quad (\text{S2})$$

- A Einstein transition coefficient (s^{-1})
 Q effective quenching rate (s^{-1})
 n_i number density of the quenching partner i (cm^{-3})
 v_{ri} relative velocity (cm/s)
 σ_I cross section (cm^2)

In case quenching coefficients instead of cross sections are given, Q is expressed as follows:

$$Q = \sum n_i k_{iq} \quad (\text{S3})$$

- k_{iq} quenching coefficient (cm^3/s)

The Einstein transition coefficient denotes the total spontaneous emission rate of the upper level, which is equal to its reciprocal lifetime. For NO(A²Σ⁺-²Π) A is taken from LIFBASE¹⁵. For NH(A³Π-X³Σ) A is taken from Zhou et al.¹⁶ The values are reported in the summary Table S1. Q is a sum over all possible quenchers, taking into account their density.

The relative speed of the quencher to the quenched molecule is calculated as follows:

$$v_{rel} = \sqrt{\frac{8kT}{\pi\mu}} \quad (S4)$$

$$\text{with } \mu = \frac{1}{\frac{1}{m_1} + \frac{1}{m_2}} = \frac{m_1 m_2}{m_1 + m_2} \text{ in (g/particle)} \quad (S5)$$

$$\text{Meaning } m_i = \frac{1}{M_i \cdot N_A} \quad (S6)$$

With:

$$k = 1.380649 \times 10^{-16} \text{ cm}^2 \text{ g} / (\text{s}^2 \text{ K}), \text{ for } v_{rel} \text{ expressed in cm/s.}$$

This also means that

$$k_{iq} = \sigma_i v_{rel} \quad (S7)$$

For both the quenching coefficients and cross-section there are a wide range of values found in literature. In this work the Q values from three sources were calculated and their average was used as the quenching coefficient. The three sets of constants are shown in Table S2.

With q known, the signal corrected for quenching is calculated using eq. 10:

$$I_{measured} = I_{original} \cdot q \quad (S8)$$

q fraction of the signal that is visible after quenching

I_{measured} measured signal

I_{original} the signal without quenching

Table S1. Einstein transitions coefficients of NH(A³Π-X³Σ) and NO(A²Σ⁺)

Einstein transition coefficient A (1/s)		
NO(A ² Σ ⁺ - ² Π)	9.8×10 ⁵	¹⁷
NH(³ Π- ³ Σ)	1.39×10 ⁶	¹⁶

Table S2. The cross sections and rate coefficients for NH(A³Π) and NO(A²Σ⁺) quenching by N₂, O₂ and H₂O as collisional quenchers.

Quencher	Cross section (NH(A ³ Π)) (cm ²)		Rate coefficient (NO(A ² Σ ⁺)) (cm ³ /s)		
	Set A	Set B	Set C	Set D	Set E

N ₂	0.1×10^{-16}	13	0.0061×10^{-16}	18	0.00047×10^{-10}	19	0.00065×10^{-10}	20	0.00074×10^{-10}	19
O ₂	1.5×10^{-16}	13	4.3×10^{-16}	18	1.47×10^{-10}	19	1.46×10^{-10}	20	1.59×10^{-10}	21
H ₂ O	9.8×10^{-16}	13	9.8×10^{-16}	18	7.71×10^{-10}	19	7.8×10^{-10}	20	7.58×10^{-10}	21

S5.2 Correction for sensitivity

The difference in light collection at different wavelengths was measured and used to correct the NH(A³Π – X³Σ) and NO(A²Σ⁺ – ²Π) band intensities. As a light source, a Hamamatsu D2 model L7293 lamp was used with a C9598 power supply.

S5.3 Correction for excitation probability

The correction for the excitation probability can be applied under the approximation that the systems behaves as assumed in the corona model. The corona approximation is a simplified approach to population densities in nonequilibrium plasmas. It assumes an equilibrium where transition upwards for ionization and excitation occurs solely through electron impact, and the transitions downwards only occurs through spontaneous emission and radiative decay. As we are working at atmospheric pressure and our averaged temperature is low, this means we do not take into account collisional recombination, 3-body recombination, step-wise excitation, charge exchange, and V-V and V-T processes.²²

Direct electron impact excitation requires electrons with an energy above 5.48 eV and 3.68 eV, for NO(A²Σ⁺ – ²Π) and NH(A³Π – X³Σ),²³ respectively. The corresponding excitation probability will be different by the following factor (eq. 11):

$$\frac{P(NO)}{P(NH)} = \frac{n_{e > 5.48 \text{ eV}}}{n_{e > 3.68 \text{ eV}}} \times \frac{\exp\left(\frac{EE_{NO}}{k_b \cdot T_e}\right)}{\exp\left(\frac{EE_{NH}}{k_b \cdot T_e}\right)} = 0.17 \times \frac{n_{e > 5.48 \text{ eV}}}{n_{e > 3.68 \text{ eV}}} \quad (S9)$$

- P probability of electron impact excitation
- n_e electron density
- T_e electron temperature
- k_b Boltzmann constant

The ratio of the density of electrons with the required energy for the excitation to NO(A²Σ⁺) and NH(A³Π) can be presented by the fraction of electrons assuming a Maxwell-Boltzmann energy distribution, which results in an excitation factor of 0.0331 for NO(A²Σ⁺) excitation compared to NH(A³Π). It has to be noted that the considered corona-model corrected for quenching processes is valid for low ionization degree plasmas with only electron impact excitation mechanisms. Additional excitation processes can lead to overestimation of the excited states density in the corona model. However, a model including a complete set of population processes would require a collisional-radiative model which is not yet available in literature for mixtures such as used in our work.

S6. NO_x formation in (humid) N_2 and air

This is a discussion based on the NO and NO_2 trends presented in Figure 2 of the manuscript. Describing the detailed reaction mechanisms for HNO_x , NO, NO_2 and NH_3 , as well as their interplay, requires dedicated computational studies based on a chemical kinetics model, which can take into account large reaction sets, while incorporating the plasma parameters (e.g., power density) as input. We did this for a much simpler chemical system consisting only of dry air²⁴, where we discussed how reverse reactions of the Zeldovich mechanism can be suppressed and the vibrational nonequilibrium can be promoted through the use of pulsed power and resulting pulsed temperature. A complete computational model with added H_2O would be much more complex, and was outside the scope of the present work. However, based on our general insights obtained from our other models, data from literature, and our present experimental data, we can hypothesize the following mechanisms.

In brief, in humid N_2 the dominating mechanism for NO and NO_2 formation is the extended Zeldovich mechanism (see RS1 in Table S3), as discussed by Gromov et al.²⁵, because H_2O is the sole oxygen source. However, the concentrations of NO and NO_2 were below 1 ppm for the whole range of used H_2O content (<1-100% relative humidity)), likely because all NO_x reacted further to form HNO_2 , as seen in Figure 2a and 2b.

On the other hand, in humid air where O_2 is readily available, the NO_x concentration is not only dramatically higher than in humid N_2 (where NO_x concentration was <1 ppm), but is up to 4 times higher than the HNO_2 concentration (e.g., 69 ppm HNO_2 , 254 ppm NO_x at 50% relative humidity and 2 L/min; Figure 2d). In this scenario, NO_x formation is guided by both the traditional non-thermal (RS2 and RS3) and the extended Zeldovich mechanisms (RS1) shown in Table S3.

Table S3. (Extended) Zeldovich reactions, their corresponding reaction rate coefficients and relevant temperature ranges.

Reaction	Rate coefficients ^a	Temperature range	Ref
$\text{N} + \text{OH} \rightarrow \text{NO} + \text{H}$	4.7×10^{-17}	300–2500 K	RS1 ²⁶
$\text{O}_2 + \text{N} \rightarrow \text{NO} + \text{O}$	$4.47 \times 10^{-12} \times e^{-27188/\text{RT}}$	298–5000 K	RS2 ²⁶
$\text{N}_2 + \text{O} \rightarrow \text{NO} + \text{N}$	$3.01 \times 10^{-10} \times e^{-318000/\text{RT}}$	1400–4000 K	RS3 ²⁶

^a Unit: $\text{cm}^3/(\text{molecules} \cdot \text{s})$ for two-body reactions, and $\text{cm}^6/(\text{molecules}^2 \cdot \text{s})$ for three-body reactions. T is the gas temperature.

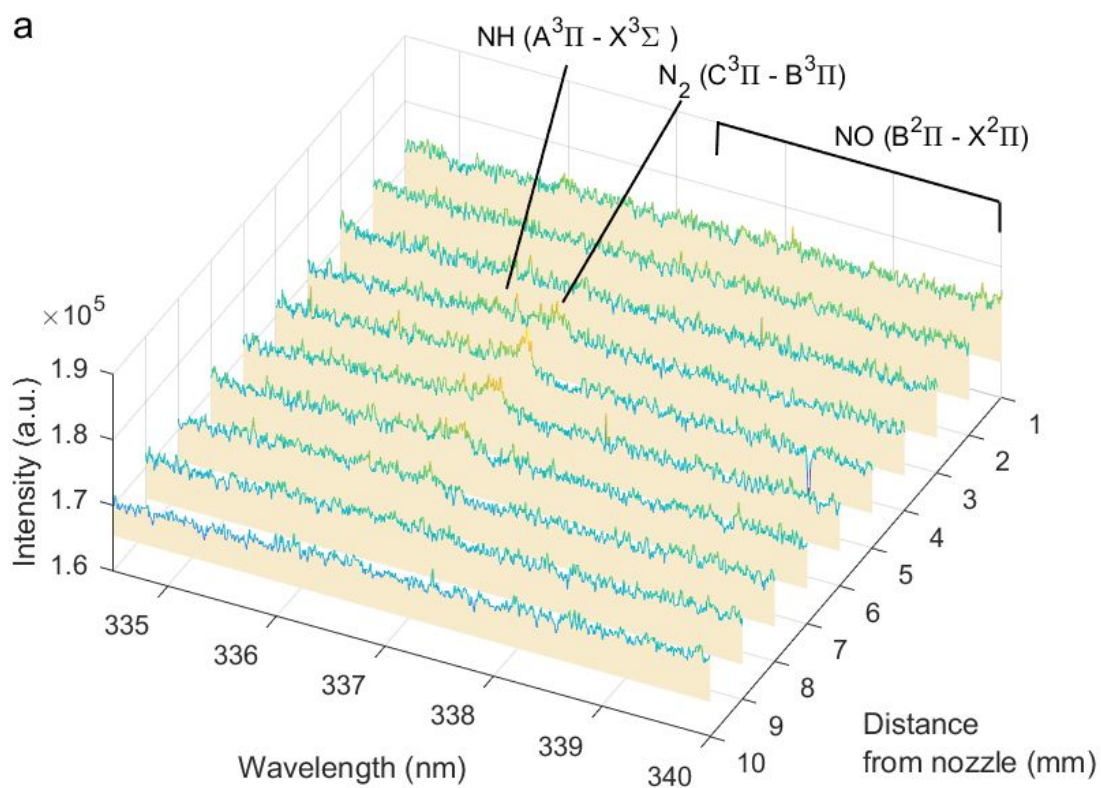
S7. OES spectra recorded perpendicular to the plasma effluent

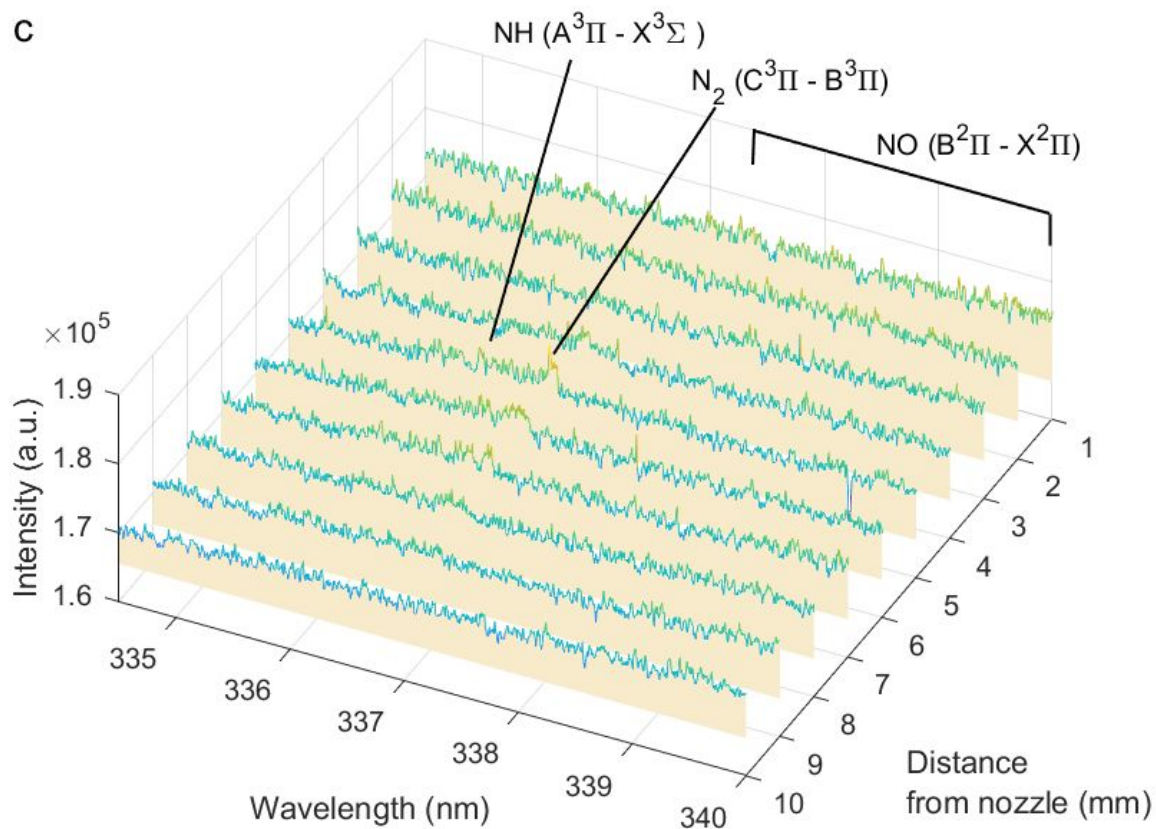
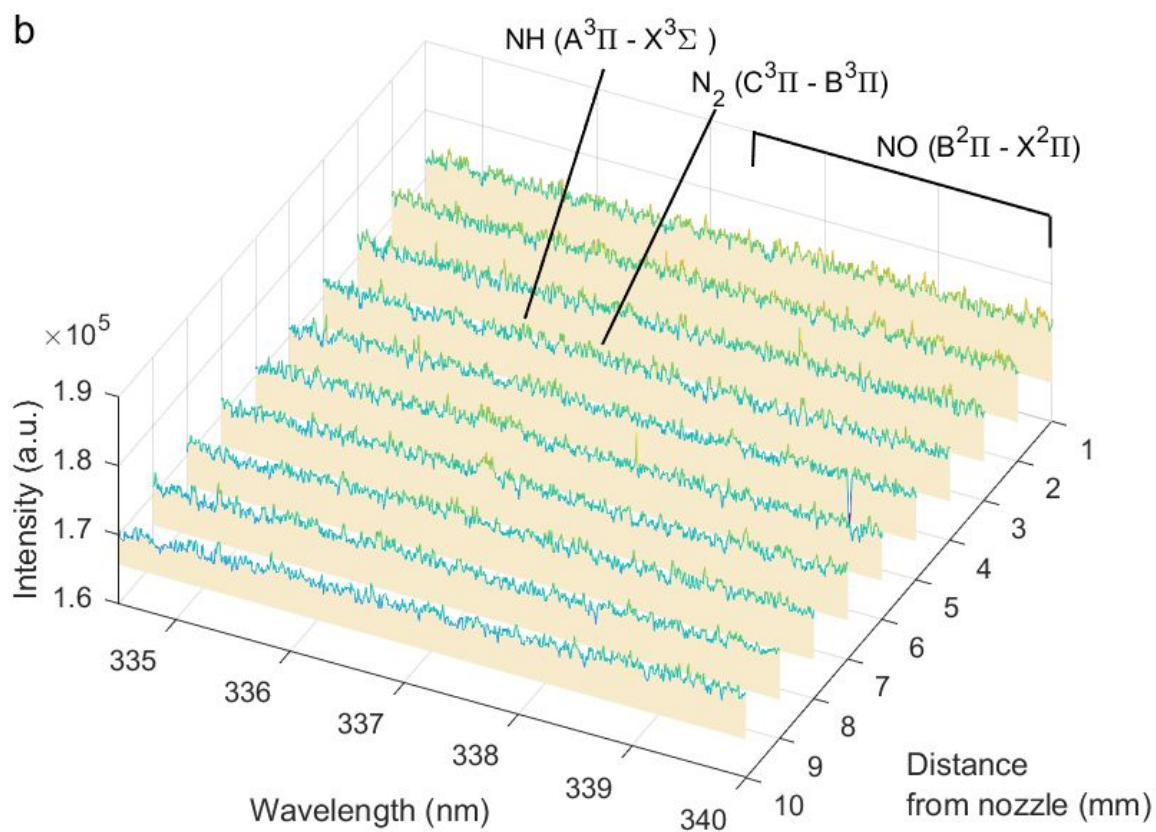
Table S4. Overview of the waterfall plot conditions and their respective Figure numbers.

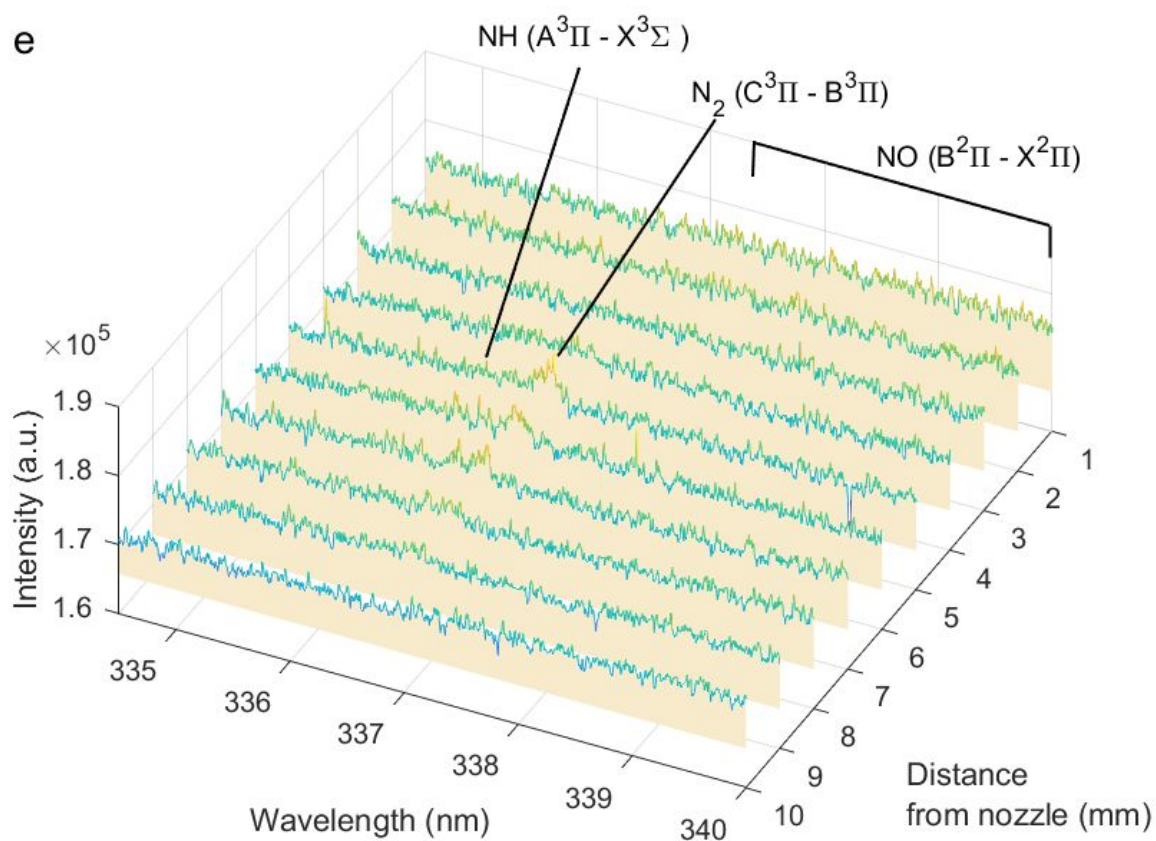
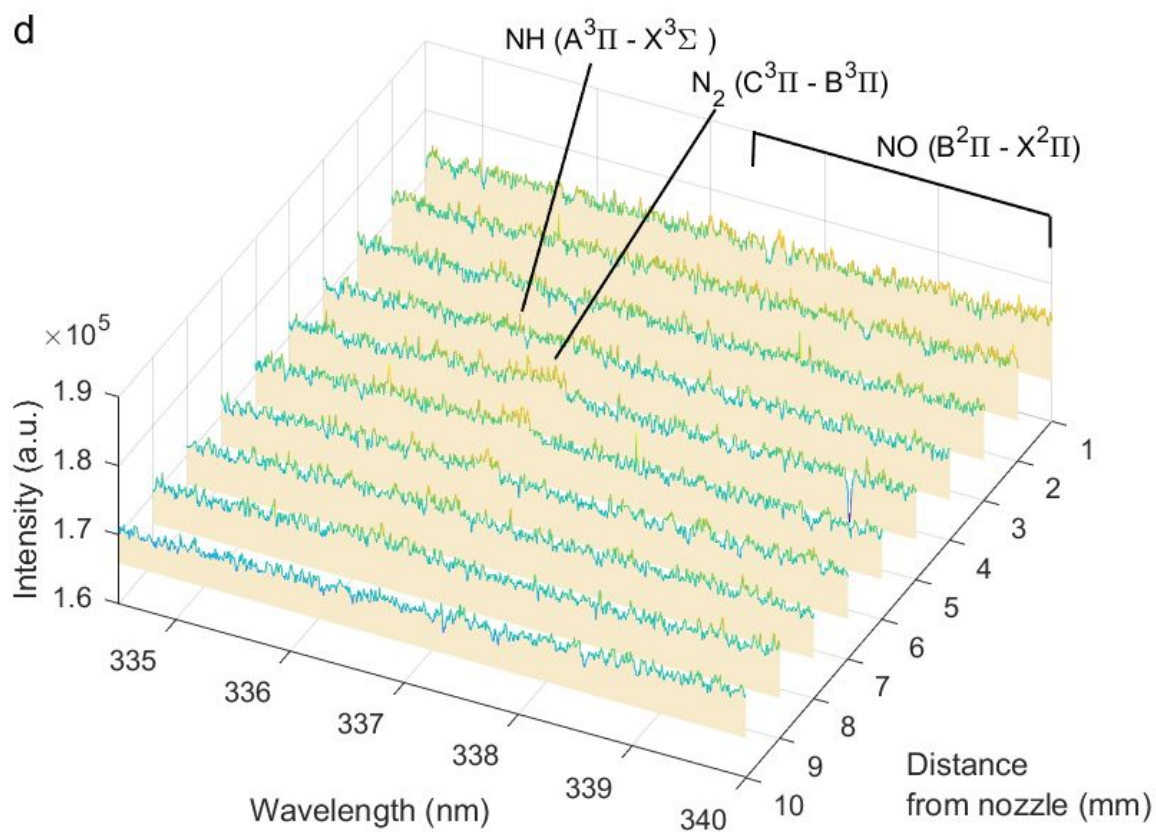
Gas	Air									
Flow rate (Slm)	0.5					2				
Relative humidity at 20°C (%)	<1	5	30	50	100	<1	5	30	50	100
Figure S4.	a	b	c	d	e	f	g	h	i	j
Gas	N_2									
Flow rate (Slm)	0.5					2				

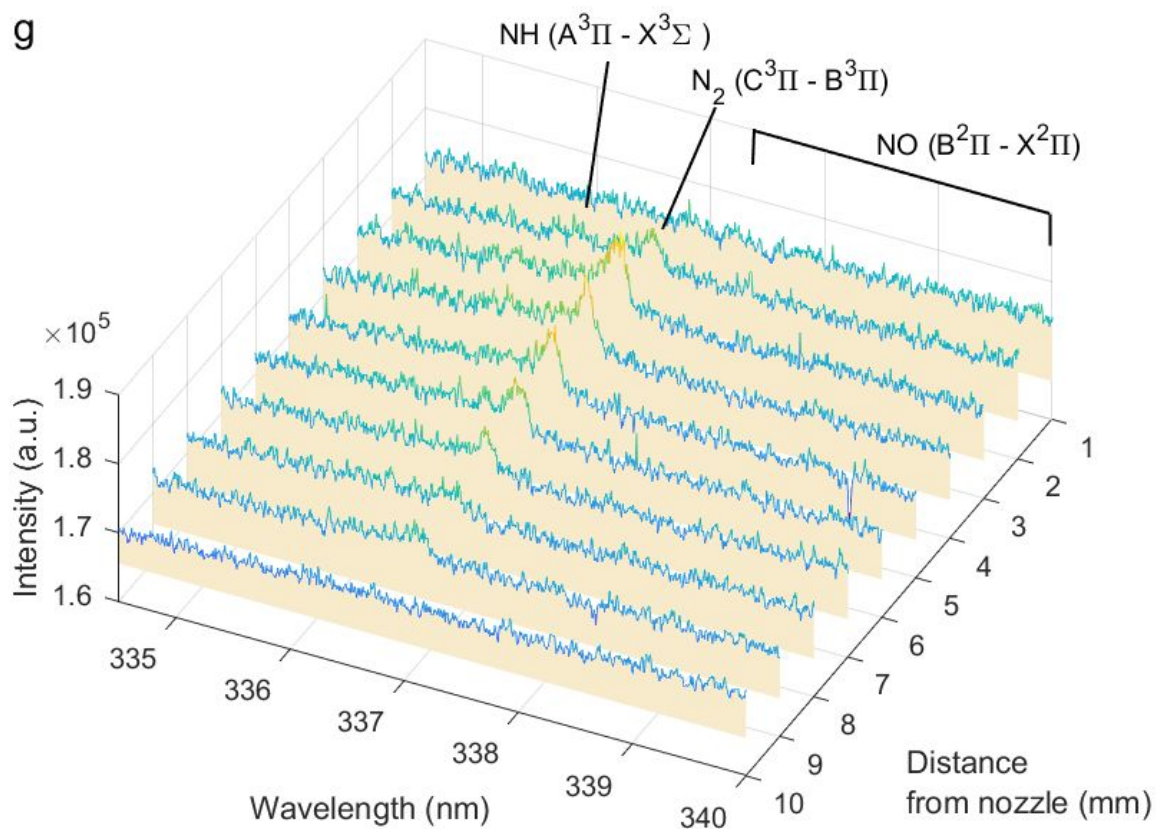
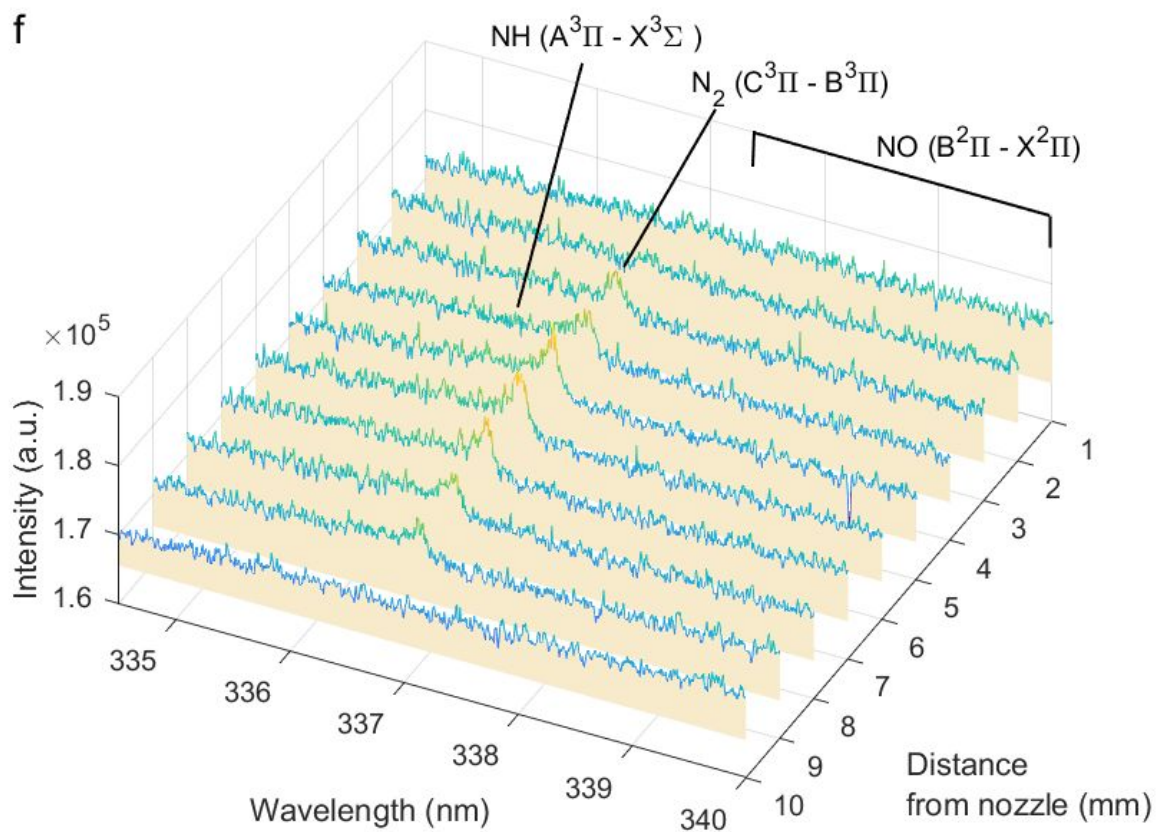
Relative humidity at 20°C (%)	<1	5	30	50	100	<1	5	30	50	100
Figure S4.	k	l	m	n	o	p	q	r	s	t

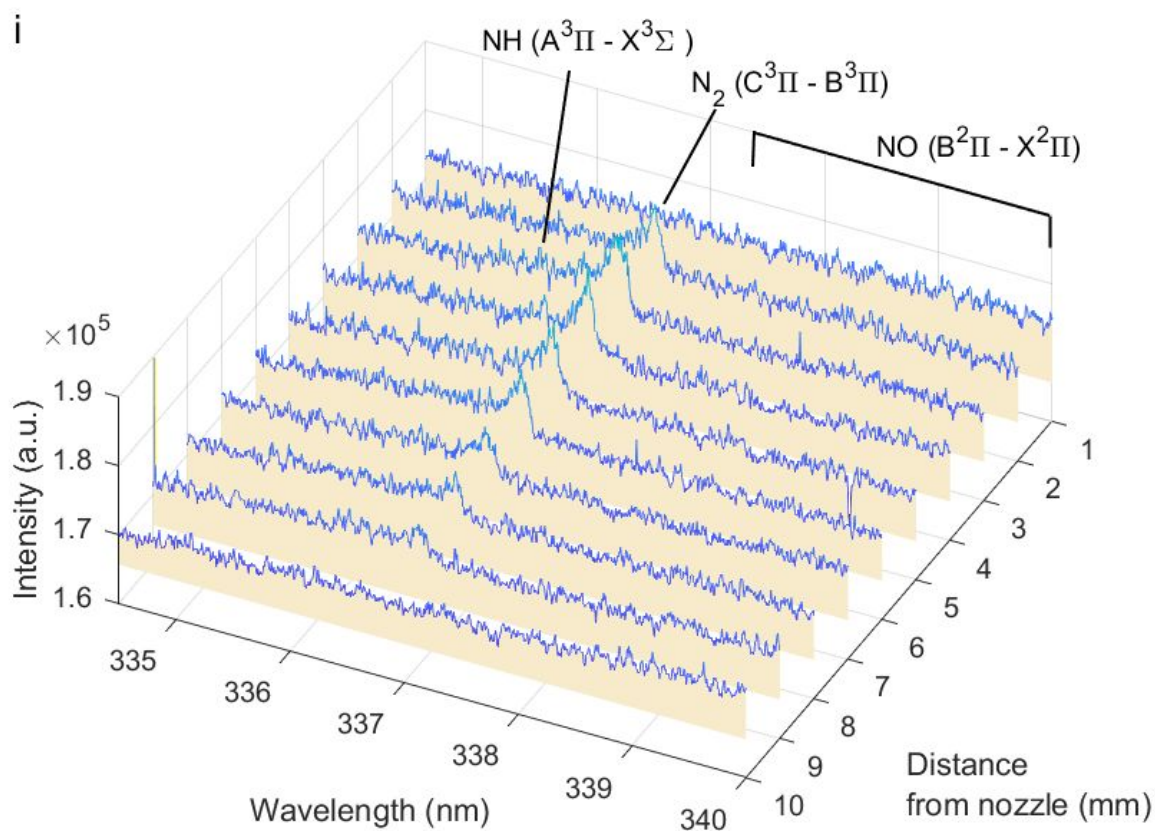
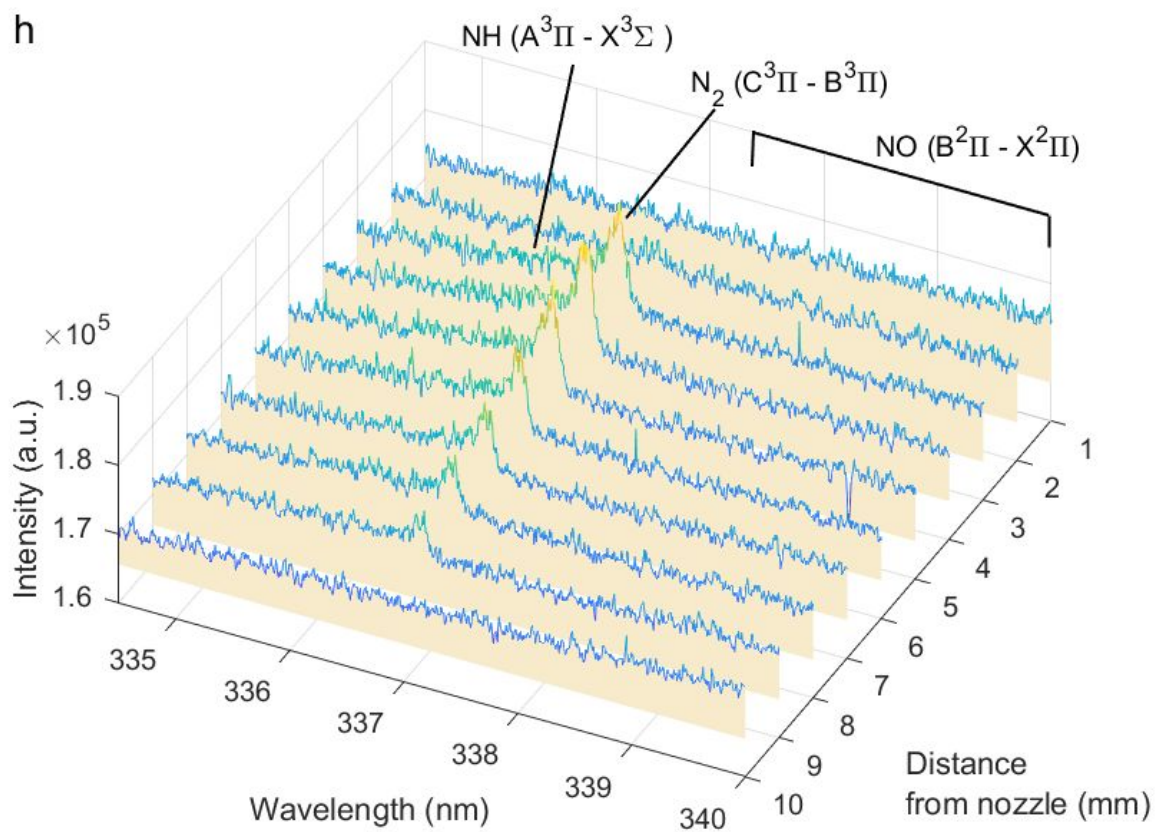
Figure S5. Emission spectra (334–340 nm) as a function of the distance from the jet nozzle (1–10 mm). The full list of the experimental conditions (Figures S5a – S5t) is shown in Table S3 above.

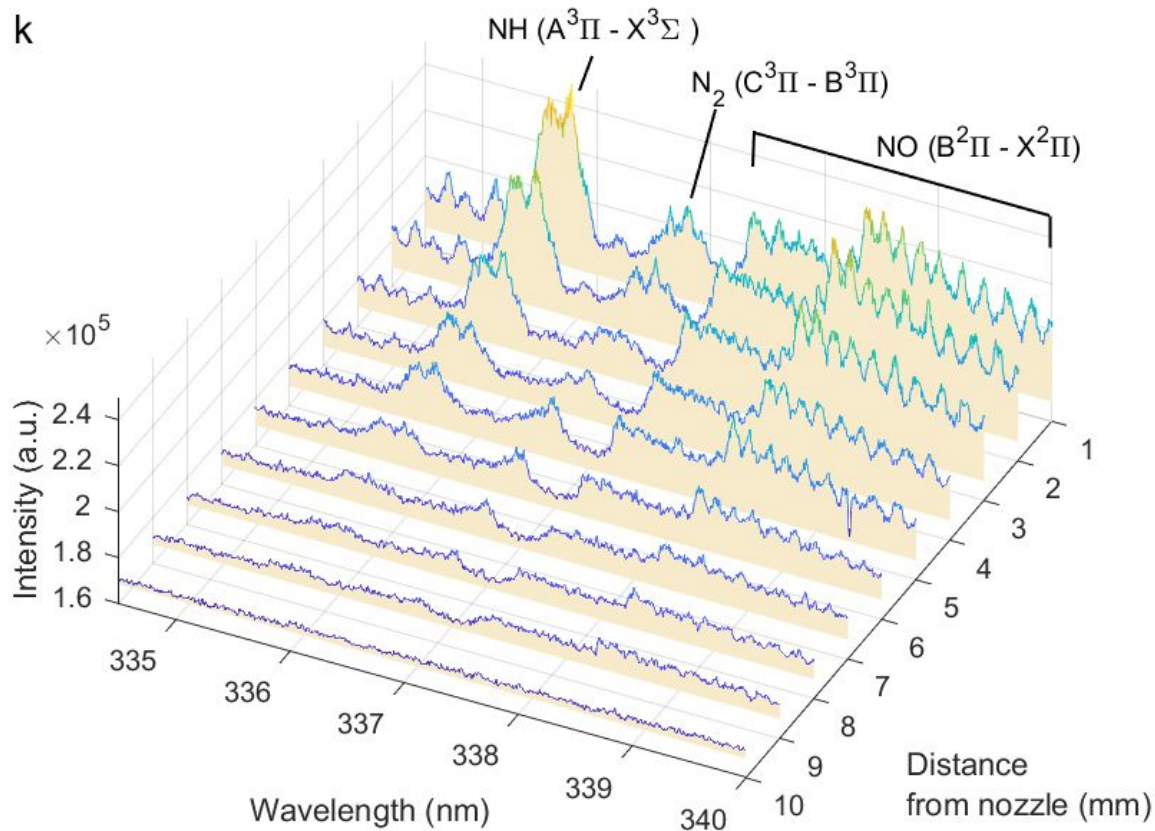
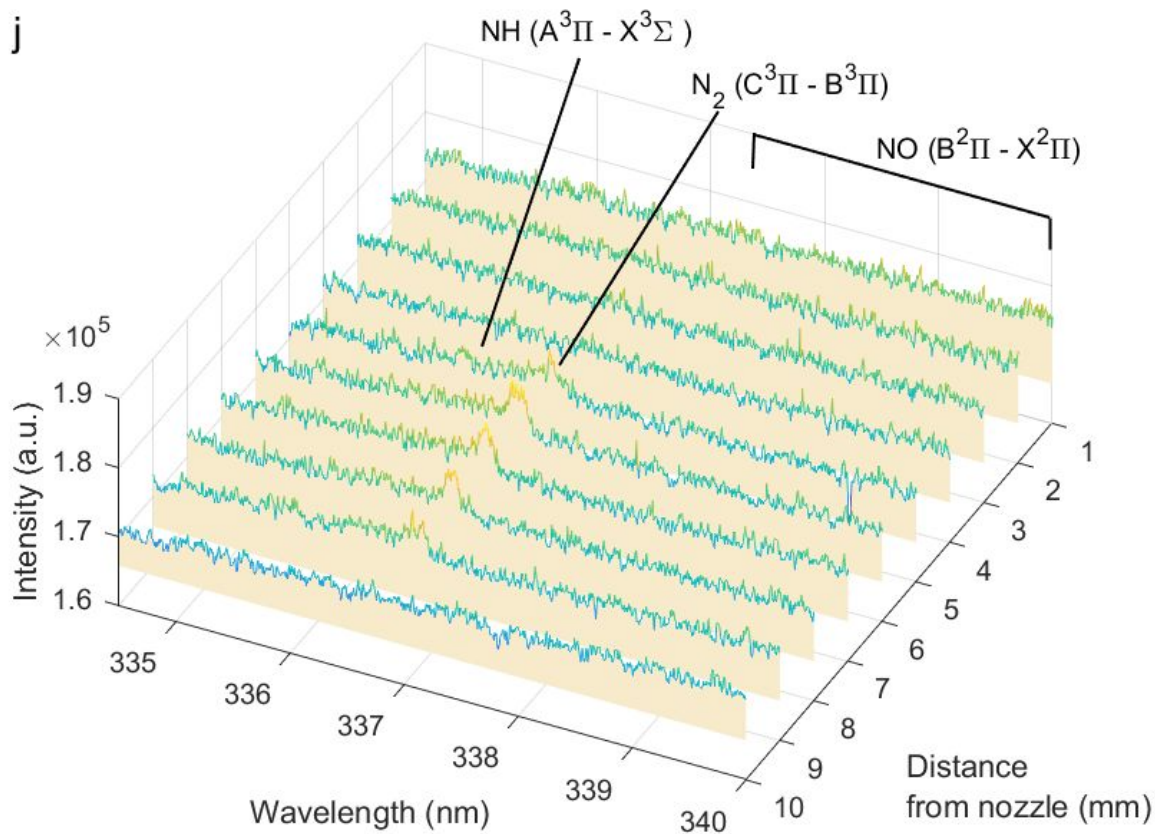


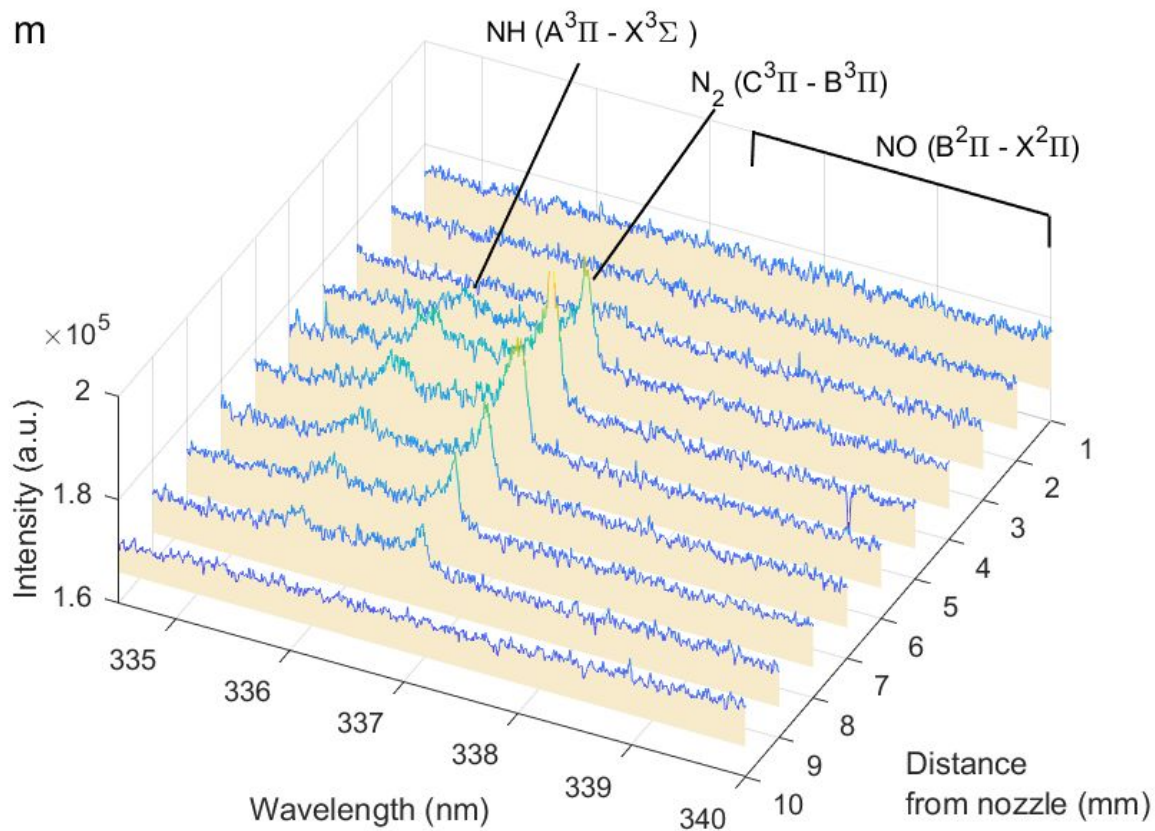
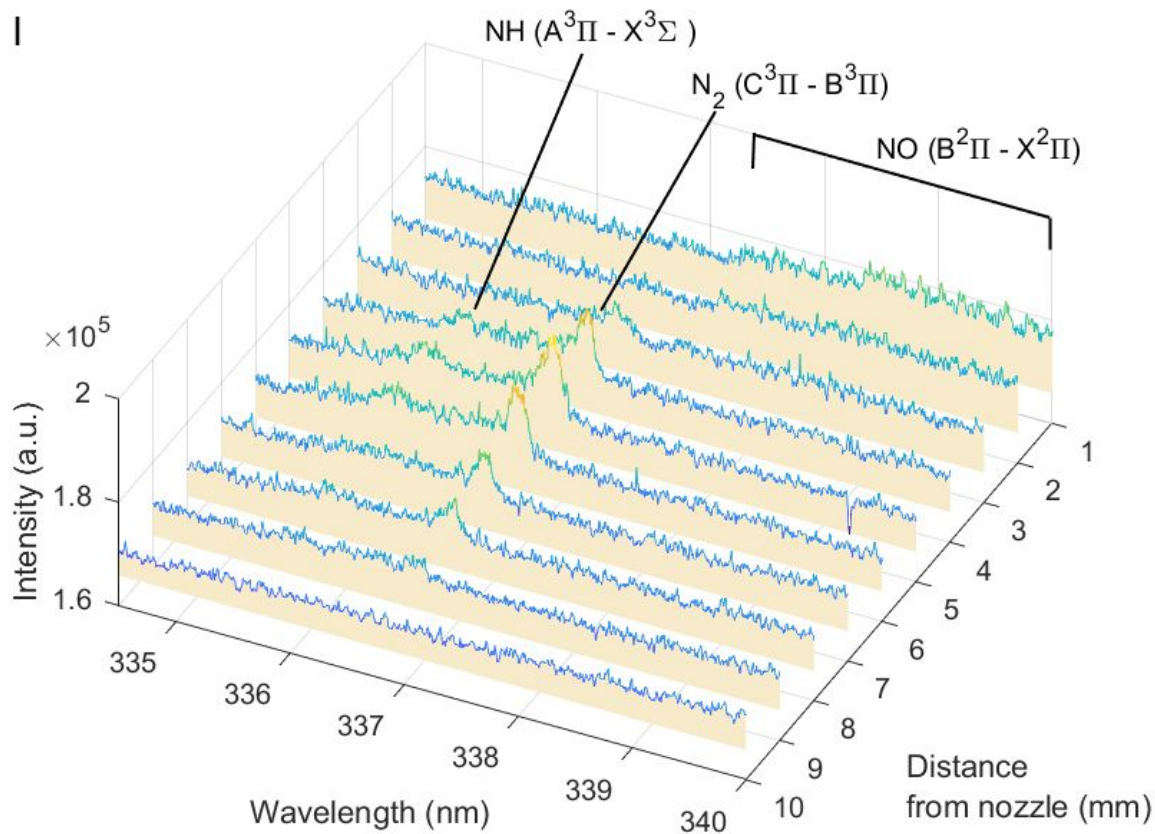


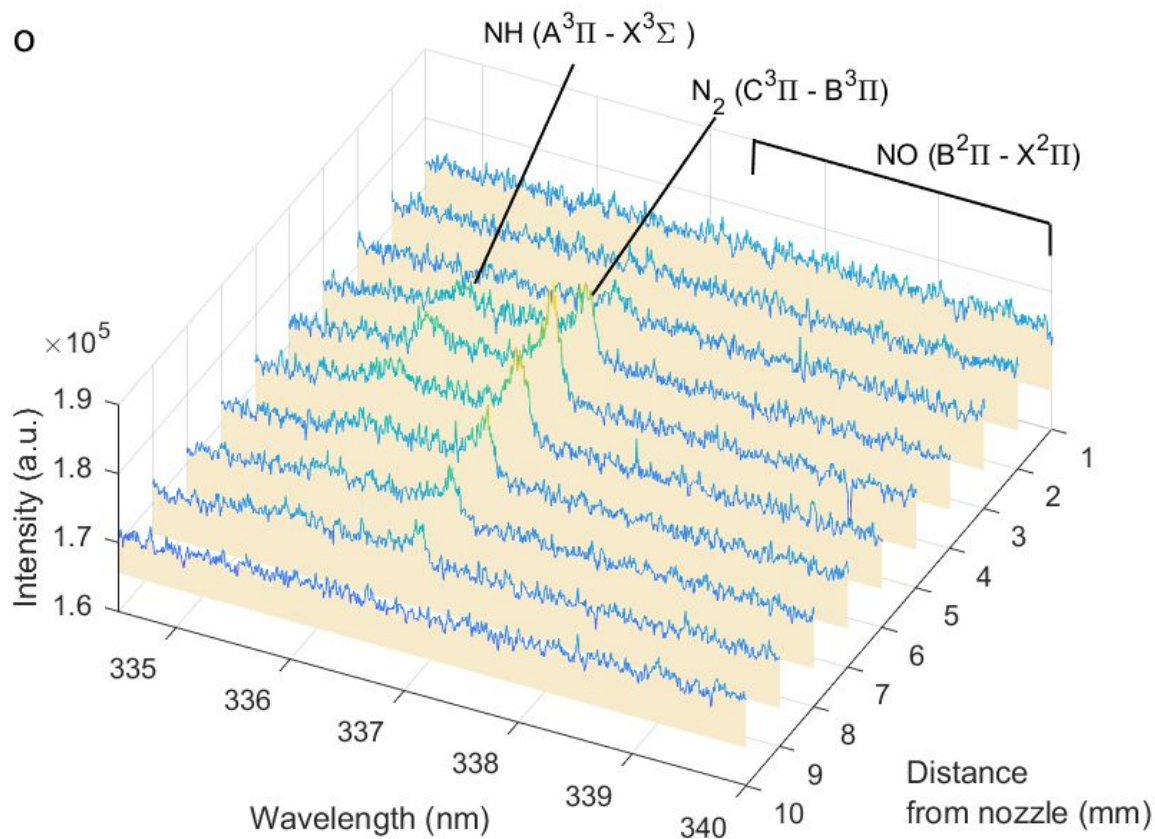
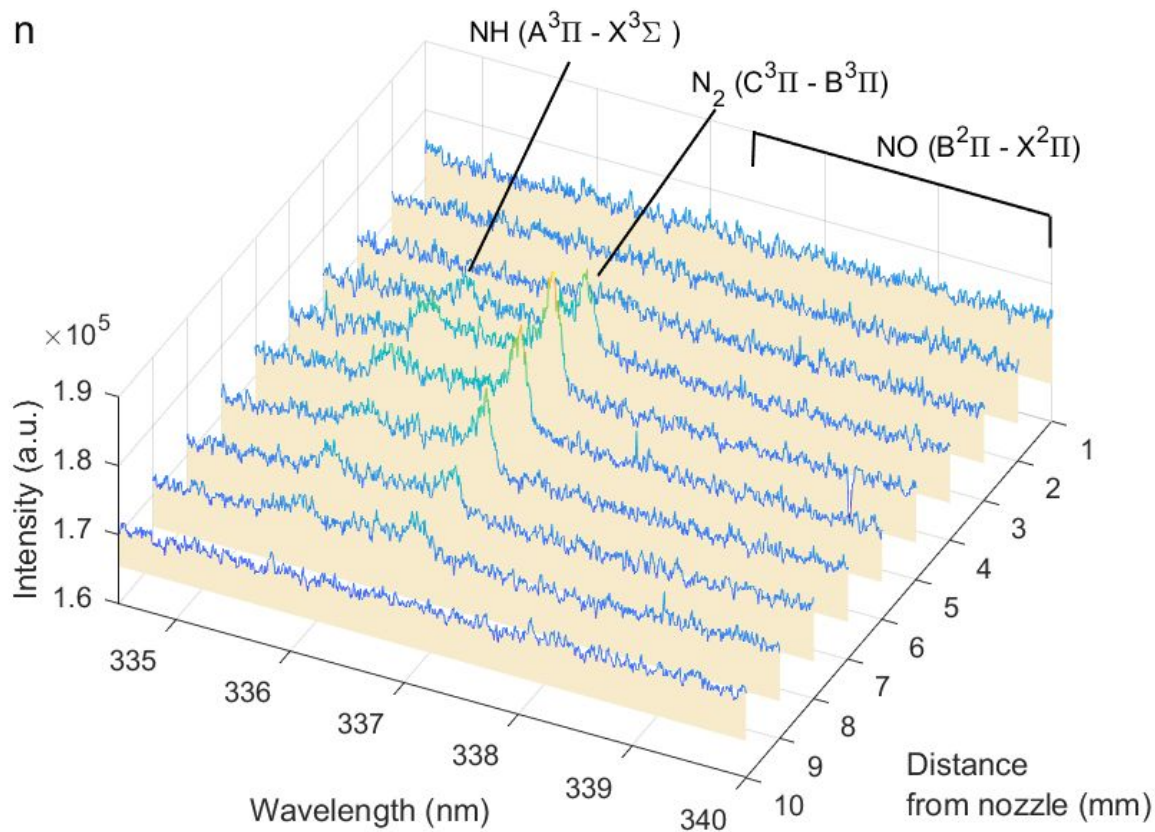


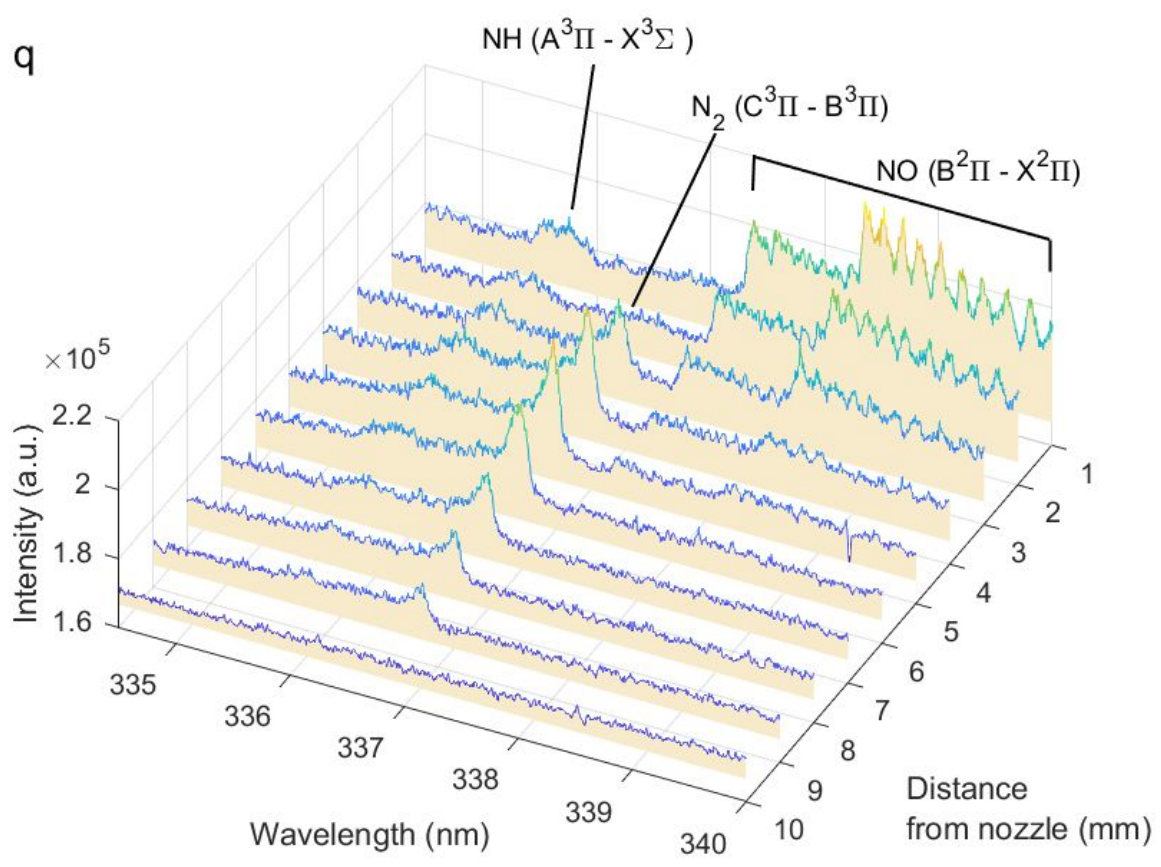
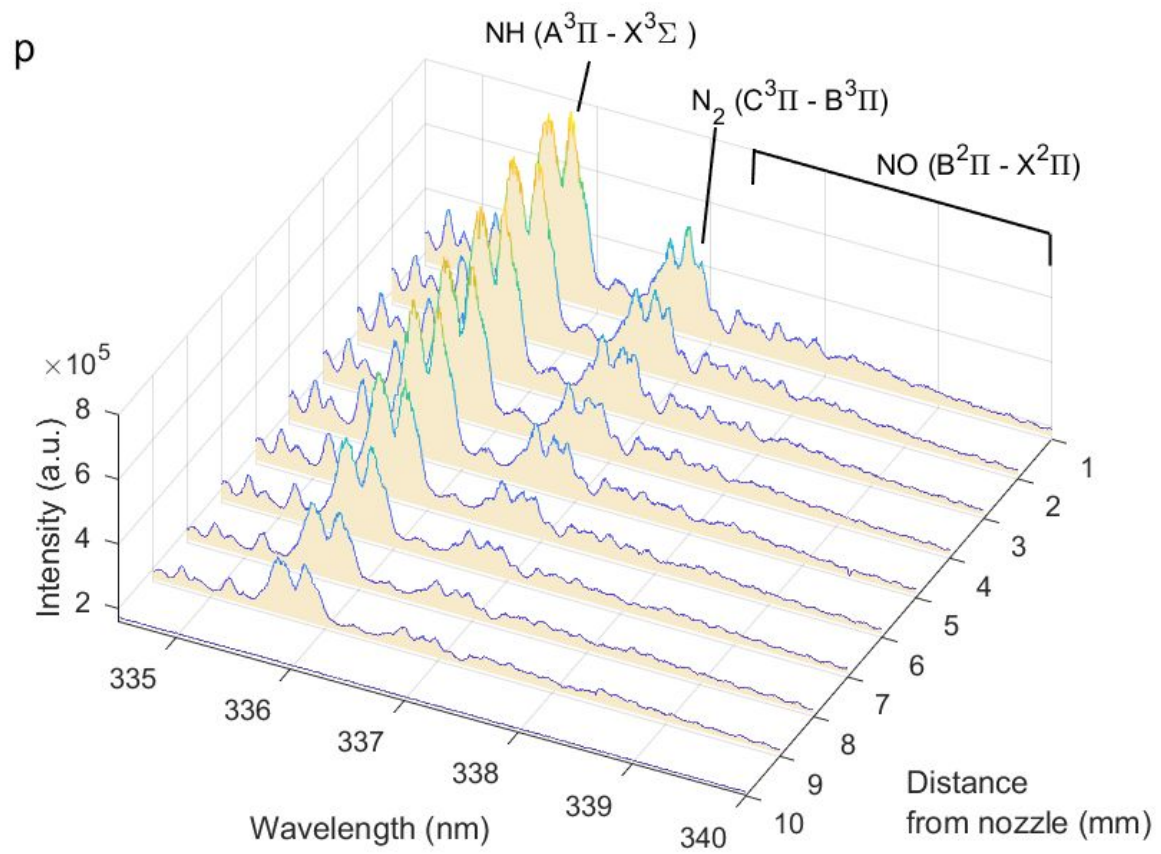


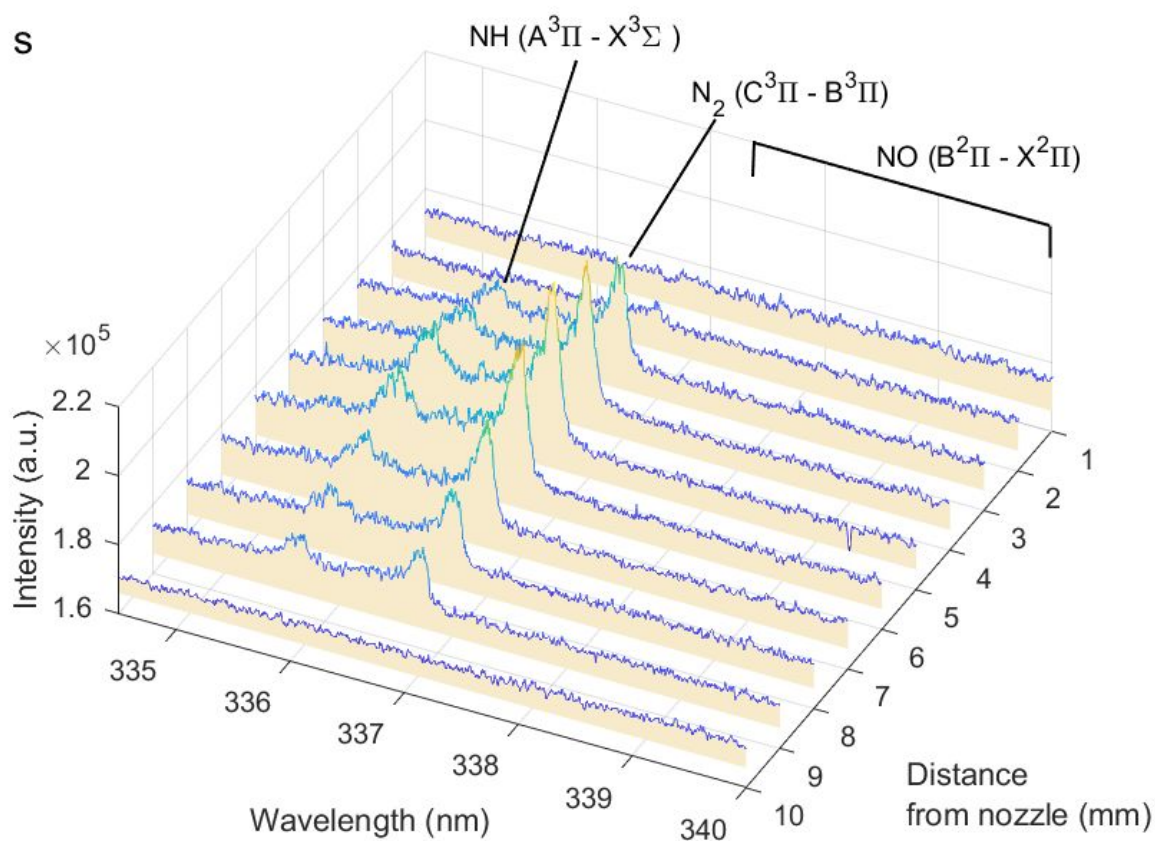
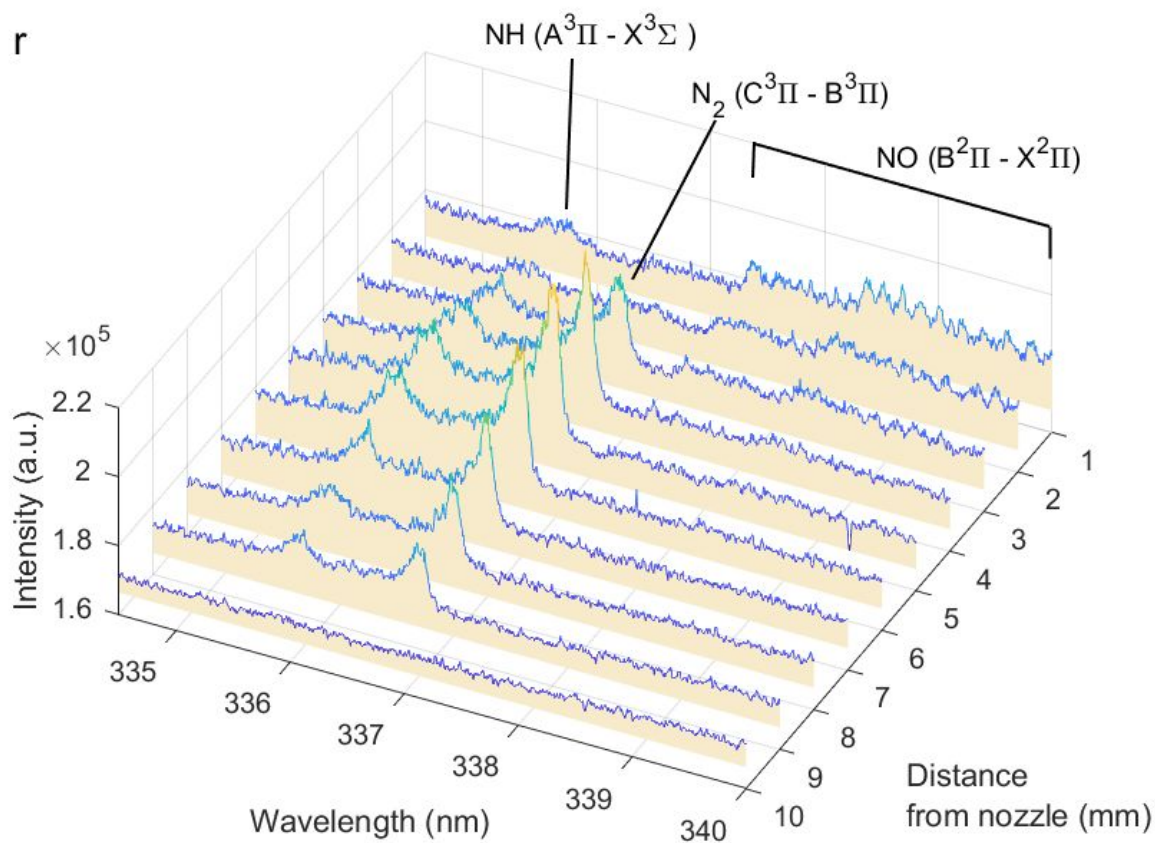


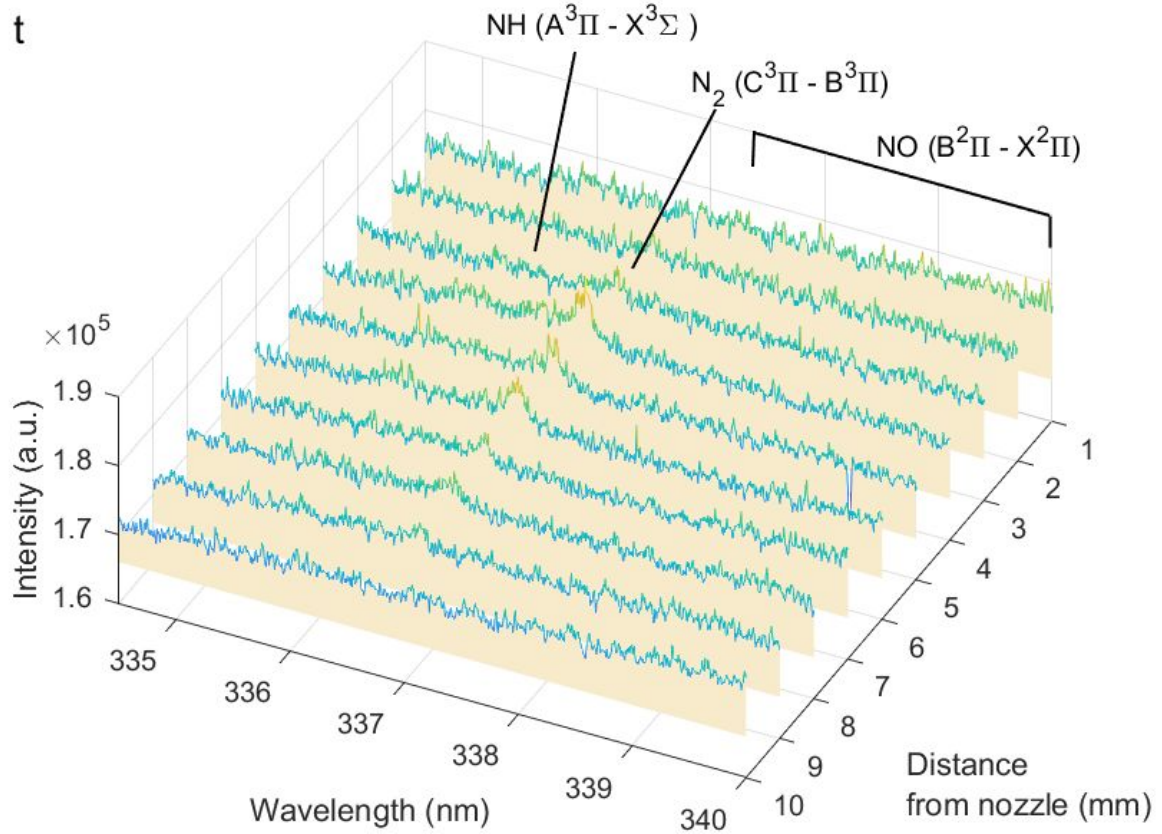












S8. Energy consumption and production rate

Using the plasma power (P) and the total (H)NO_x concentration, the EC was calculated according to eq. 12. The EC is expressed in MJ/(mol N), where mol N is the amount of nitrogen fixed. The power was close to constant for all conditions, as discussed in detail elsewhere^{24,27}, hence in the first approximation the same plug power (1.04 W) was used for all conditions.

$$\begin{aligned}
 EC \left(\frac{MJ}{mol N} \right) &= \frac{P(W)}{\text{mol of (H)NO}_x \text{ produced per second} \left(\frac{mol}{s} \right)} \times \frac{1}{10^6 \left(\frac{J}{MJ} \right)} \\
 &= \frac{P(W) \times 10^6 \times 60 \left(\frac{s}{min} \right) \times 22.4 \left(\frac{L}{mol} \right)}{(C_{HNO_2} + C_{NO_2} + C_{NO} + C_{NH_3}) \text{ (ppm)} \times \text{Flowrate} \left(\frac{L}{min} \right) \times 10^6 \left(\frac{J}{MJ} \right)} \quad (S10)
 \end{aligned}$$

The detailed methodology of energy consumption calculations is given in our previous work.²⁴ It has to be emphasized here that for clarity of the results we only report the total energy consumption, which can be drastically improved by optimization of the power supply system. As shown in our previous results, both experimentally and numerically, the plasma power

which is used to support the sustaining of the discharge, can be a factor of magnitude lower than the total power. The engineering challenge is to design a power system where power efficiency is optimized which is however out of the scope of our current research. Note that the values of the plasma EC look much better, i.e., with values of 0.42 MJ/(mol N fixed)²⁴, but they don't account for the power supply efficiency, and for real application, the total EC should be considered.

As seen from the data, even the lowest EC we observed is still ca. 4 times higher than the EC of Haber-Bosch, which is 0.48 MJ/(mol N). Nonetheless, plasma has the advantage of being able to use renewable electricity, because of its fast switch on/off capacity, and is therefore promising for distributed fertilizer production. We infer that plasma processes should be used as an auxiliary technology, rather than substituting the current industrial state-of-the-art entirely.

Table S5. Average energy consumption (EC) of nitrogen fixation.

Flow rate (L/min)	Relative Humidity (%)	EC (MJ/(mol N fixed))	
		Air	N ₂
0.5	<0.1	5.54	-
	5	5.40	238.01
	30	5.03	192.28
	50	4.79	78.25
	100	6.12	59.22
	2	<0.1	4.45
2	5	3.37	106.03
	30	2.93	43.13
	50	2.18	22.03
	100	2.70	60.76

The production rate (PR) of the various products (x), and the conversion of N₂ in our system was calculated as shown in eq. 13 and 14:

$$PR_x \left(\frac{mg}{h} \right) = \frac{C_x \text{ (ppm)} \times \text{Flow rate} \left(\frac{L}{min} \right) \times 60 \left(\frac{min}{h} \right)}{22.4 \left(\frac{L}{mol} \right) \times 10^3} \times M_x \left(\frac{g}{mol} \right) \quad (S11)$$

$$N_2 \text{ conversion (\%)} = \frac{(C_{HNO_2} + C_{NO_2} + C_{NO} + C_{NH_3}) \text{ (ppm)}}{N_2 \text{ fraction in the feed gas (ppm)} \times 2} \times 100\% \quad (S12)$$

Table S6. Average production rate (PR) of the products of nitrogen fixation, and the conversion of N₂

Flow Rate (L/min)	Relative Humidity (%)	PR (mg/h)								N ₂ conversion (%)	
		Air				N ₂				Air	N ₂
		NO	NO ₂	NH ₃	HNO ₂	NO	NO ₂	NH ₃	HNO ₂		
0.5	<0.1	18	3.4	-	-	-	-	-	-	0.032	-
	5	17	2.7	-	1.8	-	-	0.20	0.19	0.032	0.00059
	30	18	2.7	-	4.2	-	-	0.14	0.53	0.035	0.00073
	50	19	2.9	-	4.0	-	-	0.21	1.3	0.037	0.0018
	100	15	1.7	-	3.5	-	-	0.21	2.39	0.029	0.0024
2	<0.1	19	9.9	-	0.0	-	-	0.00	0.00	0.010	-
	5	23	11	-	5.1	-	-	0.51	0.26	0.013	0.00033
	30	23	11	-	14	-	-	0.92	1.5	0.015	0.00081
	50	37	6.1	-	17	-	-	0.76	4.2	0.020	0.0016
	100	29	5.3	-	15	-	-	0.00	2.9	0.016	0.00058

We note that the EC and PR values shown are not compensated for the losses due to the NH₄NO₂ decomposition and NH₄NO₃ precipitation because the experiments with the alkaline washer were not performed for every condition used.

REFERENCES

- (1) Gordon, I. E.; Rothman, L. S.; Hargreaves, R. J.; Hashemi, R.; Karlovets, E. v.; Skinner, F. M.; Conway, E. K.; Hill, C.; Kochanov, R. v.; Tan, Y.; Wcisło, P.; Finenko, A. A.; Nelson, K.; Bernath,

- P. F.; Birk, M.; Boudon, V.; Campargue, A.; Chance, K. v.; Coustenis, A.; Drouin, B. J.; Flaud, J. M.; Gamache, R. R.; Hodges, J. T.; Jacquemart, D.; Mlawer, E. J.; Nikitin, A. v.; Perevalov, V. I.; Rotger, M.; Tennyson, J.; Toon, G. C.; Tran, H.; Tyuterev, V. G.; Adkins, E. M.; Baker, A.; Barbe, A.; Canè, E.; Császár, A. G.; Dudaryonok, A.; Egorov, O.; Fleisher, A. J.; Fleurbaey, H.; Foltynowicz, A.; Furtenbacher, T.; Harrison, J. J.; Hartmann, J. M.; Horneman, V. M.; Huang, X.; Karman, T.; Karns, J.; Kass, S.; Kleiner, I.; Kofman, V.; Kwabia-Tchana, F.; Lavrentieva, N. N.; Lee, T. J.; Long, D. A.; Lukashchuk, A. A.; Lyulin, O. M.; Makhnev, V. Y.; Matt, W.; Massie, S. T.; Melosso, M.; Mikhailenko, S. N.; Mondelain, D.; Müller, H. S. P.; Naumenko, O. v.; Perrin, A.; Polyansky, O. L.; Raddaoui, E.; Raston, P. L.; Reed, Z. D.; Rey, M.; Richard, C.; Tóbiás, R.; Sadiq, I.; Schwenke, D. W.; Starikova, E.; Sung, K.; Tamassia, F.; Tashkun, S. A.; vander Auwera, J.; Vasilenko, I. A.; Viganò, A. A.; Villanueva, G. L.; Vispoel, B.; Wagner, G.; Yachmenev, A.; Yurchenko, S. N. The HITRAN2020 Molecular Spectroscopic Database. *J. Quant. Spectrosc. Radiat. Transf.* **2022**, *277*, 107949. DOI 10.1016/j.jqsrt.2021.107949.
- (2) Engeln, R.; Klarenaar, B.; Guaitella, O. Foundations of Optical Diagnostics in Low-Temperature Plasmas. *Plasma Sources Sci Technol* **2020**, *29* (6). DOI 10.1088/1361-6595/ab6880.
 - (3) MacKie, D. M.; Jahnke, J. P.; Benyamin, M. S.; Sumner, J. J. Simple, Fast, and Accurate Methodology for Quantitative Analysis Using Fourier Transform Infrared Spectroscopy, with Bio-Hybrid Fuel Cell Examples. *MethodsX* **2016**, *3*, 128–138. DOI 10.1016/j.mex.2016.02.002.
 - (4) Bacsik, Z.; Mink, J.; Keresztury, G. FTIR Spectroscopy of the Atmosphere. I. Principles and Methods. *Appl. Spectrosc. Rev.* **2004**, *39* (3), 295–363. DOI 10.1081/ASR-200030192.
 - (5) Bacsik, Z.; Mink, J.; Keresztury, G. FTIR Spectroscopy of the Atmosphere Part 2. Applications. *Appl. Spectrosc. Rev.* October 2005, pp 327–390. DOI 10.1080/05704920500230906.
 - (6) Pipa, A. v.; Ropcke, J. Analysis of the Mid-Infrared Spectrum of the Exhaust Gas from an Atmospheric Pressure Plasma Jet (APPJ) Working with an Argon-Air Mixture. *IEEE Trans. Plasma Sci.* **2009**, *37* (6), 1000–1003. DOI 10.1109/TPS.2009.2013865.
 - (7) Cantrell, C. A.; Davidson, J. A.; McDaniel, A. H.; Shetter, R. E.; Calvert, J. G. Infrared Absorption Cross Sections for N₂O₅. *Chem. Phys. Lett.* **1988**, *148* (4), 358–363. DOI 10.1016/0009-2614(88)87288-9.
 - (8) Maki, A. G.; Sams, R. L. Diode Laser Spectra of Cis-HONO near 850 Cm⁻¹ and Trans-HONO near 1700 Cm⁻¹. *J. Mol. Struct.* **1983**, *100*, 215–221. DOI 10.1016/0022-2860(83)90093-5.
 - (9) van Duc Long, N.; Al-Bared, M.; Lin, L.; Davey, K.; Tran, N. N.; Pourali, N.; Ken Ostrikov, K.; Rebrov, E.; Hessel, V. Understanding Plasma-Assisted Ammonia Synthesis via Crossing Discipline Borders of Literature: A Critical Review. *Chem. Eng. Sci.* **2022**, *263*, 118097–118110. DOI 10.1016/j.ces.2022.118097.
 - (10) Itikawa, Y. Cross Sections for Electron Collisions with Ammonia. *J. Phys. Chem. Ref. Data* **2017**, *46* (4), 043103–043111. DOI 10.1063/1.5001918.
 - (11) Pearse, R. W. B.; Gaydon, A. G. *Identification of Molecular Spectra*; Chapman & Hall LTD: London, 1950; Vol. Second Edition. DOI 10.1021/ed041pA398
 - (12) Itikawa, Y. Cross Sections for Electron Collisions with Nitric Oxide. *J. Phys. Chem. Ref. Data* **2016**, *45* (3), 033106–033115. DOI 10.1063/1.4961372.

- (13) Buckley, S. G.; Damm, C. J.; Vitovec, W. M.; Anne Sgro, L.; Sawyer, R. F.; Koshland, C. P.; Lucas, D. Ammonia Detection and monitoring with Photofragmentation Fluorescence. *Appl. Opt.* **1998**, *37*, 8382–8391. DOI 10.1364/AO.37.008382.
- (14) Hartinger, K. T.; Nord, S.; Monkhouse, P. B. Quenching of Fluorescence from Na(3 2 P) and K(4 2 P) Atoms Following Photodissociation of NaCl and KCl at 193 Nm. *Appl. Phys. B* **1997**, *64*, 363–367. DOI 10.1007/s003400050185
- (15) J. Luque; D.R. Crosley. LIFBASE: Database and Spectral Simulation Program . SRI International 1999. DOI 10.1063/1.480064
- (16) Zhou, M.; Zhu, Z. Properties of Transitions between X3Σ⁻, A3Π, A1Δ, B1Σ⁺, and C1Π States of NH Radicals. *Comput. Theor. Chem.* **2021**, *1204*, 113458–113468. DOI 10.1016/J.COMPTC.2021.113358.
- (17) Luque, J.; Crosley, D. R. Transition Probabilities and Electronic Transition Moments of the A2Σ⁺ - X2Π and D2Σ⁺ - X2Π Systems of Nitric Oxide. *J. Chem. Phys.* **1999**, *111* (16), 7405–7415. DOI 10.1063/1.480064.
- (18) Hofzumahaus, A.; Stuhl, F. Electronic Quenching, Rotational Relaxation, and Radiative Lifetime of NH(A3Π, V'=0, N'). *J. Chem. Phys.* **1984**, *82* (7), 3152–3159. DOI 10.1063/1.448213.
- (19) Tamura, M.; Berg, P. A.; Harrington, J. E.; Luque, J.; Jeffries, J. B.; Smith, G. P.; Crosley, D. R. Collisional Quenching of CH(A), OH(A), and NO(A) in Low Pressure Hydrocarbon Flames. *Combust Flame* **1998**, *114* (3–4), 502–514. DOI 10.1016/S0010-2180(97)00324-6.
- (20) Greenblatt, G. D.; Ravishankara, A. R. Collisional Quenching of NO(A, v' =0) by Various Gases. *Chem. Phys. Lett.* **1987**, *136* (6), 501–505. DOI 10.1016/0009-2614(87)80506-7.
- (21) Paul, P. H.; Gray, J. A.; Durant, J. L.; Thoman, J. W. Collisional Electronic Quenching Rates for NO (A2σ⁺ v' = 0). *Chem. Phys. Lett.* **1996**, *259*, 508–514. DOI 10.1016/0009-2614(96)00763-4.
- (22) Fantz, U. Basics of Plasma Spectroscopy. *Plasma Sources Sci. Technol.* **2006**, *15* (4), S137–S147. DOI 10.1088/0963-0252/15/4/S01.
- (23) Mo, Y.; Ottinger, C.; Shen, G. Collision-Induced Intersystem Crossing from NH(A1Δ, b 1Σ⁺) to NH(A3Π): Gateway-Mediated and Direct Mechanisms. *J. Chem. Phys.* **1999**, *111* (10), 4598–4612. DOI 10.1063/1.479221.
- (24) Vervloessem, E.; Gorbanev, Y.; Nikiforov, A.; de Geyter, N.; Bogaerts, A. Sustainable NOx Production from Air in Pulsed Plasma: Elucidating the Chemistry behind the Low Energy Consumption †. *Green Chem.* **2022**, *24*, 916–929. DOI 10.1039/d1gc02762j.
- (25) Gromov, M.; Leonova, K.; de Geyter, N.; Morent, R.; Snyders, R.; Britun, N.; Nikiforov, A. N2oxidation Kinetics in a Ns-Pulsed Discharge above a Liquid Electrode. *Plasma Sources Sc. Technol.* **2021**, *30* (6), 65024–65038. DOI 10.1088/1361-6595/abff71.
- (26) Baulch, D. L.; Cobos, C. J.; Cox, R. A.; Frank, P.; Hayman, G.; Just, Th.; Kerr, J. A.; Murrells, T.; Pilling, M. J.; Troe, J.; Walker, R. W.; Warnatz, J. Evaluated Kinetic Data for Combustion Modelling. Supplement I. *J. Phys. Chem. Ref. Data* **1994**, *23*, 847–1033. DOI 10.1063/1.555953.

- (27) Gorbanev, Y.; Vervloessem, E.; Nikiforov, A.; Bogaerts, A. Nitrogen Fixation with Water Vapor by Nonequilibrium Plasma: Toward Sustainable Ammonia Production. *ACS Sust. Chem. Eng.* **2020**, *8*, 2996–3004. DOI 10.1021/acssuschemeng.9b07849.